Impact of silver addition on the superconducting performances of $Bi_2Sr_2Ca_{0.925}Na_{0.075}Cu_2O_y$:Ag composite fibers

B. Atilla[1], I. Ergin[1], M. Gürsul[*1], B. Özçelik[*1], M.A. Madre[2], and A. Sotelo[2]

[1] *Department of Physics, Faculty of Sciences and Letters, Çukurova University, 01330 Adana, Turkey*
[2]*INMA (CSIC-Universidad de Zaragoza), Maria de Luna, 50018 Zaragoza, Spain*

Abstract

This work studies the impact of metallic Ag addition on the microstructural, electrical, superconducting, and magnetic properties of $Bi_2Sr_2Ca_{0.925}Na_{0.075}Cu_2O_y$. Samples with 0, 1, 3, 5 wt.% were prepared from precursors produced by sol-gel method, followed by texturing through the laser floating zone (*LFZ*) technique. These samples were then subjected to annealing, due to their incongruent melting, to obtain the superconducting phase. Powder XRD patterns showed that samples were mainly composed by Bi-2212 phase and metallic Ag. These data were confirmed through SEM-EDS, which also showed that samples have very low porosity and good grain orientation. The normal state and residual resistivity values decrease with Ag addition up to 3 wt.% (from 7.61 to 2.54, and from 1.85 to 0.25 mΩ.cm, respectively), reflecting the reduction of porosity and the improvement of grains alignment and connectivity. Flux pinning energies (*U*) of samples increase with Ag addition (from 0.4 to 0.5 eV under 0 T) and decrease with higher magnetic fields. Irreversibility line (*IL*) shifts towards high temperature with the introduction of Ag, confirming the higher grains connectivity in Ag-containing samples. Moreover, the increase of H_{irr} (from 28.9 to 43.1 T), H_{c2} (from 64.6 to 85.9 T), and J_c (from 0.4 10^5 to 1.2 10^5 A/cm^2) values with Ag addition also point out to the improvement of grains connectivity and flux pinning energies induced by Ag addition.

Keywords: Bi-2212, magneto-resistivity, flux pinning energy, TAFF, Irreversibility field

Corresponding authors:
e-mail: mgursul@cu.edu.tr; ozcelik@cu.edu.tr

1. Introduction:

Among high temperature superconductors (HT_c), one of the most studied is the Bi-Sr-Ca-Cu-O system (*BSCCO*), discovered by Maeda and his group [1]. It has a general chemical formula $Bi_2Sr_2Ca_{n-1}Cu_nO_{2n+4+\delta}$, where n=1, 2, and 3, indicating the number of CuO_2 layers in the crystallographic unit cell. Depending on the n value, BSCCO system consists of three different phases, Bi-2201 (n=1), Bi-2212 (n=2), and Bi-2223 (n=3), with 20, 85, and 110 K critical temperatures (T_c), respectively [1,2]. Among these phases, the Bi-2212 is the most used in technological applications due to its stability in a wide range of compositions, and processing temperatures. However, several issues may restrict their electrical transport properties: i) formation of weak links between grains [3]; ii) formation of secondary phases along the grain boundaries, and iii) weak flux pinning properties resulting from intrinsic defects in the lattice structure.

Some strategies used to overcome these issues and enhance the transport properties of these compounds are based on the addition of metallic elements which can modify the phase equilibria without reacting with the superconducting phase [4-6] and enhance density, critical current density (J_c), and critical magnetic field (H_c). Another possibility is based on the modification of charge carrier concentration in the Cu-O planes and/or enhancing the grain alignment [7-12], which can influence critical temperature, critical current density (J_c), and critical magnetic field (H_c). The most usual techniques to produce the grain alignment in the bulk materials are spark plasma texturing [13], hot uniaxial pressing [14], the Laser Floating Zone (LFZ) [15], and the Electrically Assisted Laser Floating Zone (EALFZ) [8]. Among these techniques, the LFZ method has many advantages for obtaining long BSCCO fibers grown at high rates. In this method, the microstructure of the materials is described by a good grain orientation with their growth direction quasi-perpendicular to the c-axis [16]. These large and highly oriented grains dramatically improve the transport properties, J_c, as a result of reduction in the number of low-angle junctions [17]. On the other hand, these compounds display incongruent melting [18] and, consequently, as-grown materials must be subjected to an annealing process for obtaining nearly pure Bi-2212 phase from the secondary ones [19]. Another drawback of these materials are their poor mechanical properties, which impose severe restrictions for technological applications. However, it has been shown that Ag addition leads to the improvement of mechanical properties of BSCCO compound [19].

When evaluating transport properties in HT_c superconductors, two-stage resistive transition behavior is found. The first one is the onset temperature (T_c^{onset}), where resistivity starts to decrease, while the other one is offset temperature (T_c^{offset}) in the tail part of the resistivity.

T_c^{onset} indicates the superconducting transition of isolated grains, while T_c^{offset} refers to intergranular coupling. This last one decreases under external applied fields due to the Lorentz force associated to motion of flux-lines, which can be classified into three regimes depending on the applied current density: flux flow (FF) ($J > J_c$), thermally activated flux flow (TAFF) ($J \ll J_c$) , and flux creep (FC) ($J \sim J_c$) [20]. On the other hand, the presence of pinning centers overcomes the Lorentz force effect, and the flux-lines can be trapped. These pinning centers may appear naturally [21], or can be artificially created using chemical doping [11,12,23-25].

This study is focused on the investigation of magneto-resistivity, irreversibility and flux pinning energy of textured $Bi_2Sr_2Ca_{0.925}Na_{0.075}Cu_2O_y$ + x wt.% Ag superconducting composites produced through a sol-gel method via nitrates, followed by LFZ texturing. Textured materials will be structurally, microstructurally, and magnetically characterized, and these characteristics will be evaluated. Moreover, the experimental data obtained through the magneto-resistivity curves recorded between 0 and 6 T external applied magnetic field will be analyzed on the basis of the TAFF model to determine their pinning characteristics.

2. Experimental Procedure

$Bi_2Sr_2Ca_{0.925}Na_{0.075}Cu_2O_y$ + x wt.% Ag, with x= 0, 1, 3, and 5, polycrystalline samples have been produced using sol-gel method from Bi_2O_3 (≥ 99.9%, Aldrich), $SrCO_3$ (98%, Panreac), $CaCO_3$ (≥ 99%, Aldrich), Na_2CO_3 (≥ 99.99%, Aldrich), CuO (98%, Panreac) and Ag (≥ 99%, Aldrich) commercial powders. They were weighed in the appropriate proportions and dissolved in a mixture of HNO_3 (Fluka, PA) and distilled water. Once a clear blue solution has been produced, adequate amounts of ethylene glycol (99%, Panreac) and citric acid (99.5%, Panreac) were added under stirring. This solution was subsequently heated to evaporate water and decompose the HNO_3 excess, producing brownish fumes. During this process, pH is raised allowing the polymerization of citric acid and ethylene glycol, forming a light blue gel which was dried at 110 °C. Further heating at 350 ºC on a hot plate produces the organic material decomposition, leaving a very fine light brown powder which has been calcined in two steps, at 750 and 800 °C for 12 h, with an intermediate manual milling. The resulting powder was cold isostatically pressed in form of cylinders (around 3 mm diameter and 100 mm length), and used as feed in a LFZ system previously described [25]. Textured bars were produced by directional solidification at 30 mm/h growth rate under continuous power Nd:YAG laser (λ = 1064 nm) radiation. In this process, seed and feed were oppositely rotated at 3, and 15 rpm, to maintain the cylindrical geometry, and homogenize the molten

zone, respectively. As-grown materials were obtained as geometrically homogeneous cylindrical fibers (~ 120 mm length and 2 mm diameter). As previously mentioned, Bi-2212 presents incongruent melting leading to a mixture of secondary phases, with minor Bi-2212 phase content, after solidification. Consequently, an annealing treatment is necessary to obtain the Bi-2212 phase in these textured rods [26]. This thermal treatment consists on two steps: heating at 860 °C for 60 hours, 800 °C for 12 hours, and quenching in air to room temperature. The experimental procedure is schematically depicted in Fig. S1.

The sol-gel process has been studied through TGA-DTA under air atmosphere analysis performed on the dry gel and the powders obtained after firing the gel. The annealed samples were structurally characterized through powder XRD diffraction. Microstructure has been studied on longitudinal polished sections of samples using a Field Emission Scanning Electron Microscopy (FESEM, Carl Zeiss Merlin) with an energy dispersive X-Ray (EDX) spectrometer. Magneto-resistivity measurements were performed between 0 and 6 Tesla using a DynaCool-9 Quantum Design PPMS system. Magnetic hysteresis loops (M-H) at 10, 20, 30, 40 and 50 K were performed in a 7304 model Lakeshore VSM. In forthcoming sections, the $Bi_2Sr_2Ca_{0.925}Na_{0.075}Cu_2O_y$ + x wt. % Ag samples are labeled as 0% Ag, 1% Ag, 3% Ag, and 5% Ag for x= 0, 1, 3, and 5, respectively.

3. Results and Discussion

Representative DTA-TGA analysis, performed on the dry gel of the 3wt.% Ag sample, is shown in Fig. S2. As it can be observed in the plot, three main zones can be distinguished in the TGA graph. The first one, between room temperature and 150 ºC corresponds to solvent evaporation, the second one, between 150 and 300 ºC can be associated to the decomposition of organic part, drastically decreasing the sample weight. This fact is confirmed by the large exothermic peak in the DTA graph shown in this figure. Finally, the third part, at higher temperatures presents a very slight weight loss due to the decomposition of $AgNO_3$ [27]. On the other hand, Fig. S3 shows the TGA-DTA graph obtained in the fired material (between 450 and 900 ºC for clarity). As it can be observed in the plot, there is nearly continuous weight loss in this temperature range, associated to the decomposition of alkaline earth carbonates. However, these carbonates decomposition temperatures are much lower than the reported for these compounds [27], and it is due to the very small particle sizes produced through the sol-gel method. Moreover, even if $CaCO_3$ presents lower decomposition temperatures than $SrCO_3$, it has been reported that the presence of Bi and Cu leads to the

preferential decomposition of $SrCO_3$ due to the high stability of the $Bi_2Sr_2CuO_x$ (Bi-2201) phase [28].

Powder XRD patterns obtained in the different samples are shown in Fig. 1a. In the graph, it can be seen that most of the peaks are associated to the Bi-2212 phase, accompanied by metallic Ag, in agreement with previous works [14,29]. Moreover, some more peaks can be observed; even if they cannot be associated to any secondary phase due to their very low intensity, previous studies showed that Bi-2201, $(Ca,Sr)CuO_2$, or $Ca_{14}Cu_{24}O_{41}$ can be found in these compounds [26].

In Fig. 1b, a representative SEM image of the 3 wt.% Ag is presented. As it can be observed, the samples show very low porosity and a good grain orientation along the growth direction. Moreover, it presents different contrasts, which have been associated to different phases through EDX, and labelled by numbers. Grey contrast (#1) corresponds to Bi-2212 phase as the major one in all samples; white and dark grey contrasts (#2, and #3) are Bi-2201, and $(Ca,Sr)CuO_2$ secondary phases, respectively; and light grey contrast (#4) corresponds to metallic Ag. In order to evaluate the microstructural modifications in the samples with Ag content, they are illustrated in Fig. S4. It is necessary to point out that Ag particles in 1% Ag samples are too small to be shown in the corresponding micrograph. The fact that Ag appears as metallic element, in agreement with the XRD data, confirms that Ag addition do not modify the chemical composition of Bi-2212 phase. On the other hand, its presence decreases the melting point of these materials due to the formation of an eutectic [29,30], which increases grain orientation due to the decrease of the radial thermal gradient [31,32]. Furthermore, a slight decrease in secondary phase content can also be observed with higher Ag content.

Variation of electrical dc resistivity as a function of temperature, between 30 and 150K for all samples is given in Fig. 2. These graphs show that all samples display metallic type behavior above T_c^{onset}. On the other hand, T_c is difficult to evaluate from this graph. Consequently, in the inset of Fig. 2, the time derivative of resistivity ($d\rho/dt$) vs temperature graph is represented. As it can be easily observed, the peak position is the same for all samples, 93.3 K, clearly showing that Ag does not modify the T_c of the Bi-2212 compounds. On the other hand, these samples show a single peak, which is associated to the very good grain coupling in these textured materials [33]. However, significant differences between the samples can be observed when fitting the high temperature part of these graphs using the well-known Mathiessen's rule, given as:

$$\rho = \rho_0 + \rho_{ep}(T) \qquad \textbf{(1)}$$

where ρ_0 is the residual resistivity which is a temperature independent coefficient associated to local structural defects, distortions, etc., and ρ_{ep} is the temperature dependent term arising from electron-phonon interaction [34,35]. ρ_0 values for these samples are determined through the extrapolation method, as shown in Fig. S5 for the 0, and 3 wt.% Ag samples, and the results are presented in Table 1, together with their estimated errors. These values clearly point out that the Ag addition up to 3 wt.% reduces distortions, defects, etc., between superconducting Cu-O_2 planes [36]. Another important parameter which can be extracted from this graph is the resistivity at 95 K, ρ_{95K}, which is influenced by impurity scattering and lattice strain through the crystal structure [37]. The data displayed in Table 1, together with their estimated error, show the same trend found for ρ_0, confirming the effect of Ag addition Finally, T_c^{onset}, T_c^{offset} and transition width (ΔT=T_c^{onset}-T_c^{offset}) can also be extracted from the graph in Fig. 2, and the results are also presented in Table 1, together with their estimated error. From these data it is easy to deduce that Ag (in the absence of magnetic field) not only modifies the superconducting transition parameters of Bi-2212 phase, but also significantly reduces the normal state (ρ_{95K}) and residual resistivity (ρ_0) values.

Magneto-resistivity characterization has been performed in the 20-140 K temperature range under different magnetic fields (0, 2, 4, and 6 T), and the obtained graphs are displayed in Fig. S6. As it can be seen in the data extracted from these graphs, with their estimated errors, shown in Table 1, while a remarkable broadening is observed in the offset part, the onset part has negligible shift with applied field. On the other hand, a serious decrease has been observed in T_c^{offset} values when the magnetic field is increased, due to the anisotropic layered crystal structure, disorder in the percolation path between grains, and high thermal energy of vortices [38,39]. Moreover, the fact that all Ag-containing samples have higher T_c^{offset} than the pristine sample indicates that Ag is a suitable conduction agent between the Bi-2212 grains, and plays an important role in reducing the broadening of resistivity curves caused by the applied field [40].

The broadening of resistivity transition in the presence of magnetic field can be explained in terms of thermally activated flux flow (TAFF) model that follows an Arrhenius-type equation [41]:

$$\rho = \rho_0 \exp(-U/k_B T) \qquad \textbf{(2)}$$

where ρ_0 is the exponential factor, U is the flux pinning or activation energy, and k_B is the Boltzman's constant. ρ_0 value corresponds to the normal resistivity value at 110 K which is physically reasonable since U is zero above T_c^{onset} [20]. The U value can be deduced from the slope of $ln\rho/\rho_0$ versus $1/T$ plots given in Fig. S7, together with their respective estimated

errors. As it can be seen in these figures, when increasing the magnetic field, the tail parts of the resistance curves shift towards lower temperatures, while the slope values of the linear parts decrease. It is well known that when increasing magnetic field, the vortices can jump to nearby pinning centers, leading to broadening in the tail part of resistivity curves. The values of U, as a function of magnetic field, are given in Fig. 3. As it can be seen in the graph, U values of all Ag-added samples are higher than the obtained for the Ag-free one in the whole measured magnetic field range, probably due to the increase in the number of pinning centers and the enhancement of intergranular coupling [42,43]. On the other hand, the U values of all samples drastically drop with the magnetic field, but this decrease is lower for Ag containing samples due to the increase of well-coupled superconducting grains in the samples [44].

Furthermore, applied magnetic field dependence of $U(H)$ can be defined by a power law as:

$$U(H) \approx H^{\beta} \quad \textbf{(3)}$$

where, β is the magnetic field orientation dependent constant with respect to basal plane [36]. By using the data plotted in Fig. 3, β values have been calculated and presented in Table 2 with their estimated errors. These data are similar to the reported in La-doped Bi-2212 samples [36] and higher than those of $BaSnO_3$-added BiPb-2223 samples [45].

The temperature dependence of $U(T)$ can be extracted from the magnetic field dependence of the transition width, and these data are shown in Fig. S8, with their estimated errors, for all samples. In the graph, it can be observed that ΔT drastically enlarges when increasing the external applied fields, due to the field penetration into the intergranular regions, reducing the superconducting current paths [45]. The dependence of ΔT on magnetic field obeys a power-law as [45],

$$\Delta T \approx H^{n} \approx H^{\beta/q} \quad \textbf{(4)}$$

By plotting ΔT versus H in log-log scale, n, β, q parameters are deduced, and displayed in Table 2, together with their respective errors. Thus, the dependence of activation energy on temperature and magnetic field can be expressed by the following equation [46].

$$U(H,T) \sim \Delta T\, H^{-\eta}; \quad \eta = \beta + n. \quad \textbf{(5)}$$

And the calculated η values are also given in Table 2, together with their errors, for all samples.

Irreversibility field (H_{irr}) of samples can be deduced from magneto-resistivity curves to obtain the irreversibility line (IL), which separates vortex glass and the vortex liquid regions in the H-T plane. In order to deduce IL of the specimens, the graph of irreversibility magnetic field values, with respect to T_c^{offset}, is displayed in Fig. S9, together with their estimated errors. It is clear from the figure that IL line shifts towards high temperature with Ag addition up to 3

wt.%, decreasing for higher content. The same behavior has been found in H_{irr} values at absolute zero, deduced from the extrapolation of the curves in Fig. S9, and presented in Table 2 for all samples, together with their estimated errors. The fact that the highest values are found in 3 wt.% Ag samples indicate that they have the strongest pinning force.

The plot of upper critical field (H_{c2}) versus the 50% value of normal resistivity (T_c midpoint) is presented in Fig. 4, with its estimated error. The zero-temperature upper critical field, $H_{c2}(0)$, values of the samples can be calculated using the Werthamer, Helfand and Hohenberg formula (WHH) given as [47]:

$$H_{c2}(0) = -0.693 T_c (dH_{c2} / dT)_{Tc} \quad \textbf{(6)}$$

According to the $H_{c2}(0)$ values shown in Table 2, $H_{c2}(0)$ gets enhanced from 64.6 T for the Ag-free samples, to 85.9 T for the 3 wt.% Ag ones, decreasing for higher Ag content.

Using the temperature dependent H_{irr} and H_{c2} curves given in Fig. S9 and Fig. 4, respectively, the vortex glass, vortex liquid and normal regions of the samples can be determined [48]. For this purpose, vortex glass, vortex liquid and normal regions of 0 and 3 wt.% Ag samples are shown in Fig. S10 with their estimated errors. This graph shows that the vortex glass transition shifts to higher temperatures, and vortex liquid region gets narrower with the addition of Ag, meaning that optimum Ag-added fibers may play a pioneering role in technological applications [34].

The magnetic hysteresis loops (*M-H*) of all samples measured under different magnetic fields, between -10 and +10 kOe, at 10, 20, 30, 40, and 50 K, are shown in Fig. S11 with their estimated errors. As it can be clearly seen in the figures, the general behavior of the *M-H* loops is strongly dependent on the Ag-amount and temperature. Furthermore, the presence of reversible and symmetrical *M-H* curves indicates that bulk pinning rather than surface barrier predominates in all samples [49]. In addition, the areas of *M-H* curves get narrower with increasing temperature as a result of the reduction of superconducting regions and the decrease of grain connectivity. On the other hand, the magnetization values at zero field, remnant magnetization, M_R, decreases when temperature is incrreased due to the reduction in the pinning strength [50]. The temperature dependence of M_R is illustrated in Fig. 5, with its estimated errors, for all samples. In this figure, it can be observed that the 3 wt.% Ag sample has the highest M_R values at all temperatures, due to their stronger pinning centers. For the purpose of comparison, the *M-H* curves of all samples at 10, 20, and 30 K are given in Fig. S12, together with their estimated error. When the figures are examined, it can be seen that the addition of silver to the system widens the *M-H* curves, when compared to the Ag-free

samples, and the widest one belongs to the 3 wt.% Ag sample at all temperatures, confirming the enhancement of intergranular connectivity and the most effective pinning centers formation.

The intergranular critical current density (J_c) values of the samples can be deduced from *M-H* loops using the Bean's model given as [51]:

$$J_c = \frac{\Delta M}{d} \qquad (7)$$

where J_c critical current density in A/cm^2, ΔM is the width of the M-H loops measured in emu/cm^3, and d is the thickness of the specimen. The calculated J_c values for all samples at 10 K are displayed in Fig. 6, and at 20, and 30 K in Fig. S13, together with their respective estimated errors. According to these data, J_c values decrease with magnetic field and temperature in all samples. However, 3 wt.% Ag sample has the highest J_c independently of temperature and applied magnetic field, confirming again that metallic Ag provides a good conduction path between the grains.

4. Conclusion

In the present work, $Bi_2Sr_2Ca_{0.925}Na_{0.075}Cu_2O_y$ + x wt. % Ag, with x= 0, 1, 3, 5 composite fibers were prepared through the sol-gel via nitrates method followed by LFZ texturing. After annealing the as-grown samples, XRD data showed that samples were mainly composed of Bi-2212 and metallic Ag, with small amounts of secondary phases. FESEM micrographs and EDX results confirmed these data, and showed good grain orientation and low porosity in these samples. Moreover, Ag particles are mainly found in the intergranular region, filling the holes between the superconducting grains. As a consequence, Ag addition reduces the normal state (ρ_{95K}) and residual resistivity (ρ_0) values in the absence of magnetic field. However, applied magnetic fields drastically reduce T_c^{offset}, especially in the Ag-free samples, confirming that metallic Ag found in the holes between the superconducting grains is a suitable conduction agent. Calculated *U* values of all Ag-added samples are higher than Ag-free one under all the measured magnetic fields. Similar trend was also observed for H_{irr}, H_{c2}, M_R, and J_c. Moreover, the best results were obtained in the 3 wt.% Ag samples, suggesting that the addition of the appropriate amount of Ag to the Bi-2212 phase is very useful to increase superconducting properties in view of its technological applications.

Acknowledgements

The results used in this manuscript has been partially taken from master thesis of B. Atilla named “Determination of Magnetoresistive Properties of $Bi_2Sr_2Ca_{0,925}Na_{0,075}Cu_2O_y$ Superconductors Added with Different Proportions of Silver (Ag)”, directed by Prof. Dr. B. Özçelik. M. A. Madre and A. Sotelo wish to thank the Gobierno de Aragón (Research Group T 54-20 R) for funding. The authors also acknowledge the use of Servicio General de Apoyo a la Investigación-SAI, Universidad de Zaragoza.

References

[1] H. Maeda, Y.Tanaka, M.Fukutumi, T.Asano, A new high-Tc oxide superconductor without a rare-earth element, Jpn. J. Appl. Phys. 27 (1988) 209.

[2] C. Michel, M. Hervieu, M. M. Borel, A. Grandin, F. Deslands, J. Provost, B. Raveav, Superconductivity in the Bi–Sr–Cu–O System, Z. Phys. B 86 (1987) 421.

[3] B. Hensel, G. Grasso, R. Flükiger, Limits to the critical transport current in superconducting $(Bi,Pb)_2Sr_2Ca_2Cu_3O_{10}$ silver-sheathed tapes: The railway-switch model, Phys. Rev. B 51 (1995) 15456.

[4] B. Ozkurt, M. A. Madre, A. Sotelo, J. C. Diez, Effect of metallic Ag on the properties of Bi-2212 ceramic superconductors, J. Mater. Sci.: Mater. Electron. 24 (2013) 3344.

[5] U. Oztornazi, B. Ozkurt, The effect of nano-sized metallic Au addition on structural and magnetic properties of $Bi_{1.8}Sr_2Au_xCa_{1.1}Cu_{2.1}O_y$ (Bi-2212) ceramics, Ceram. Int. 43 (2017) 4545.

[6] B. Ozkurt, Structural, Electric and Magnetic Properties of $Bi_2Sr_2Ag_{0.03}Ca_1Cu_2O_y$ Ceramics Modified by Post-annealing, J. Supercond. Nov. Magn. 31 (2018) 2459.

[7] M. Gürsul, A. Ekicibil, B. Özçelik, M.A. Madre, A. Sotelo, Sintering Effects in Na-Substituted Bi-(2212) Superconductor Prepared by a Polymer Method, J. Supercond. Nov. Magn. 28 (2015) 1913.

[8] F. M. Costa, Sh. Rasekh, N. M. Ferreira, A. Sotelo, J. C. Diez, M. A. Madre, Effect of current polarity on BSCCO/Ag ceramics textured by Electrically Assisted Laser Floating Zone, J. Supercond. Nov. Magn. 26 (2013) 943.

[9] B. Oner, P. Ozkurt, M. A. Madre, B. Ozkurt, A. Sotelo, Enhanced superconducting properties in $Bi_2Sr_2CaCu_{1.75}Na_{0.25}O_y$ ceramics prepared by hot-pressing under different pressures and temperatures, J. Supercond. Nov. Magn. 2022 (In press). DOI: 10.1007/s10948-022-06211-x

[10] B. Ozkurt, Enhancement in superconducting transition temperature and Jc values in Na-doped $Bi_2Sr_2Ca_1Cu_{2-x}Na_xO_y$ superconductors, J. Mater. Sci. Mater. Electron. 24 (2013) 2426.

[11] B. Özçelik, M. Gürsul, A. Sotelo, M.A. Madre, Improvement of superconducting properties in Na-doped BSCCO superconductor, J. Mater. Sci. Mater. Electron. 26 (2015) 441.

[12] B. Özçelik, M. Gürsul, A. Sotelo, M.A. Madre, Improvement of the intergranular pinning energy in the Na-doped Bi-2212 superconductors, J. Mater. Sci.: Mater. Electron. 26 (2015) 2830.

[13] L. Perez-Acosta, E. Govea-Alcaide, J. G. Noudem, I. F. Machado, S. H. Masunaga, R. F. Jardim, Highly dense and textured superconducting $(Bi,Pb)_2Sr_2Ca_2Cu_3O_{10+\delta}$ ceramic samples processed by spark-plasma texturing, Ceram. Int. 42 (2016) 13248.

[14] F. Karahman, A. Sotelo, M. A. Madre, J. C. Diez, B. Ozkurt, Sh. Rasekh, Relationship between microstructure and superconducting properties in hot-pressed Bi-2212/Ag ceramic composites, Ceram. Int. 41 (2015) 14924.

[15] Y. Huang, G. F. de la Fuente, A. Sotelo, A. Badía, F. Lera, R. Navarro, C. Rillo, R. Ibañez, D. Beltrán, F. Sapiña, A. Beltrán, $(Bi,Pb)_2Sr_2Ca_2Cu_3O_{10+\delta}$ superconductor composites ceramics vs fibers, Physica C185 (1991) 2401.

[16] G. F. de la Fuente, M. T. Ruiz, A. Sotelo, A. Larrea, R. Navarro, Microstructure of laser floating zone (LFZ) textured (Bi, Pb)-Sr-Ca-Cu-O superconductor composites, Mater. Sci. Eng. A 173 (1993) 201.

[17] D. Shi, High Temperature Superconducting Materials Science and Engineering, Pergamon Press, Oxford, 1995.

[18] K. Schulze, P. Majewski, B. Hettich, G. Petzow, Phase equilibria in the system Bi_2O_3-SrO-CaO-CuO with emphasis on the High-T_C superconducting compounds, Z. Metallkd. 81 (1990) 836.

[19] A. Sotelo, M. Mora, M. A. Madre, J. C. Diez, L. A. Angurel, G. F. de la Fuente, Ag distribution in thick Bi-2212 floating zone textured rods, J. Eur. Ceram. Soc. 25 (2005) 2947.

[20] D. Sharma, R. Kumar, V. P. S. Awana, Temperature and field dependence of thermally activated flux flow resistance in $Bi_2Sr_2CaCu_2O_{8+\delta}$ superconductor, Solid State Commun. 152 (2012) 941.

[21] J. Trastoy, V. Rouco, C. Ulysse, R. Bernard, G. Faini, J. Lesueur, J. Briatico, J. E. Villegas, Nanostructuring of high-T_C superconductors via masked ion irradiation for efficient ordered vortex pinning, Physica C 506 (2014) 195.

[22] H. Gündoğmuş, B. Özçelik, B. Özkurt, A. Sotelo, M. A. Madre, Physical, Mechanical and Magnetic Properties of the Yb-Substituted $Bi_2Sr_2Ca_1Cu_2O_y$ Textured Superconductor, J. Supercond. Nov. Magn. 26 (2013) 111.

[23] A. Özaslan, B. Özçelik, B. Özkurt, A. Sotelo, M. A. Madre, Structural, Electrical, and Magnetic Properties of the Co-Substituted Bi-2212 System Textured by Laser Floating Zone Technique, J. Supercond. Nov. Magn. 27 (2014) 53.

[24] B. Özçelik, M. Gürsul, A. Sotelo, M. A. Madre, Effect of K substitution on Structural, Electrical and Magnetic Properties of Bi-2212 system, J. Mater. Sci. Mater. Electron. 25 (2014) 4476.

[25] B. Özçelik, B. Özkurt, M. E. Yakinci, A. Sotelo, M. A. Madre, Relationship between annealing time and magnetic properties in Bi-2212 textured composites, J. Supercond. Nov. Magn. 26 (2013) 873.

[26] F. M. Costa, R. F. Silva, J. M. Vieira, Phase transformation kinetics during thermal annealing of LFZ Bi–Sr–Ca–Cu–O superconducting fibers in the range 800–870°C, Physica C 323 (1999) 23.

[27] W. M. Haynes, ed., CRC handbook of chemistry and physics, CRC Press/Taylor and Francis, Boca Raton, FL. 2016.

[28] A. Sotelo, G. F. de la Fuente, F. Lera, D. Beltrán, F. Sapiña, R. Ibañez, A. Beltrán, M. R. Bermejo, Novel Polymer Solution Synthesis of $(Bi_{1-x}Pb_x)_2Sr_2Ca_2Cu_3O_{10+\delta}$, Chem. Mater. 5 (1993) 851.

[29] P. Majewski, A. Sotelo, H. Szillat, S. Kaesche, F. Aldinger, Phase diagram studies in the system Ag-"$Bi_2Sr_2CaCu_2O_8$", Physica C 275 (1997) 47.

[30] P. Majewski, Phase diagram studies in the system Bi-Pb-Sr-Ca-Cu-O-Ag, Supercond. Sci. Technol. 10 (1997) 453.

[31] M. F. Carrasco, V. S. Amaral, R. F. Silva, F. M. Costa, Electrical assisted laser floating zone (EALFZ) growth of 2212-BSCCO superconducting fibres, Appl. Surf. Sci. 257 (2011) 5283.

[32] M. F. Carrasco, R. F. Silva, J. M. Vieira, F. M. Costa, Pulling rate and current intensity competition in an electrically assisted laser floating zone, Supercond. Sci. Technol. 22 (2009) 065016.

[33] R. Jha, H. Kishan,V. P. S. Awana, Superconducting and magneto-transport properties of BiS_2 based superconductor $PrO_{1-x}F_xBiS_2$ (x = 0 to 0.9), J. Appl. Phys. 115 (2014) 013902.

[34] A. T. Ulgen, T. Turgay, C. Terzioglu, G. Yildirim, M. Oz, Role of Bi/Tm substitution in Bi-2212 system on crystal structure quality, pair wave function and polaronic states, J. Alloy. Compd. 764 (2018) 755.

[35] P. B. Allen., W. Pickett, H. Krakauer, Anisotropic normal-state transport properties predicted and analyzed for high-Tc oxide superconductors, Phys. Rev. B 37 (1988) 7482.

[36] Y. Zalaoglu, G. Yildirim, H. Buyukuslu, N. K. Saritekin, A. Varilci, C. Terzioglu, O. Gorur, Important defects on pinning of 2D pancake vortices in highly anisotropic Bi-2212 superconducting matrix with homovalent Bi/La substitution, J. Alloy. Compd. 631 (2015) 111.

[37] G. Yildirim, Determination of optimum diffusion annealing temperature for Au surface-layered Bi-2212 ceramics and dependence of transition temperatures on disorders, J. Alloy. Compd. 699 (2017) 247.

[38] M. Rupp, A. Gubta, C. C. Tsuei, Magnetic field induced broadening of the resistive transition in epitaxial c-axis-oriented $HgBa_2CaCu_2O_{6+\delta}$ films, Appl. Phys. Lett. 67 (1995) 291.

[39] E. Hannachi, Y. Slimani, A. Ekicibil, A. Manikandan, F. B. Azzouz, Magneto-resistivity and magnetization investigations of YBCO superconductor added by nano-wires and nano-particles of titanium oxide, J. Mater. Sci. Mater. Electron. 30 (2019) 8805.

[40] B. A. Malik, M. A. Malik, K. Asokan, Magneto transport study of YBCO: Ag composites, Curr. Appl. Phys. 16 (2016) 1270.

[41] T. T. M. Palstra, B. Batlogg, R. B. van Dover, L. F. Schneemeyer, J. V. Waszczak, Dissipative flux motion in high-temperature superconductors, Phys. Rev. B 4, (1990) 6621

[42] G. Yildirim, Formation of artificial flux pinning centers in Bi-2223 cuprate superconductor with Ni impurities and enhanced resistant to thermal fluxon motions of correlated 2D pancake vortices in new matrix, J. Alloy. Compd. 745 (2018) 100.

[43] P. Rani, A. Pal, V. P. S Awana, High field magneto-transport study of $YBa_2Cu_3O_7$:Agx (x=0.00–0.20), Physica C 497 (2014) 19.

[44] E. Govea-Alcaide, I. García-Fornaris, P. Muné, R. D. Jardim, Improvement of the intergranular pinning energy in uniaxially compacting $(Bi\text{-}Pb)_2Sr_2Ca_2Cu_3O_{10+\delta}$ ceramic samples, Eur. Phys. J. B 58 (2007) 373.

[45] M. Me. Barakat, K. Habanjar, Magnetoresistivity studies for BiPb-2223 phase added by $BaSnO_3$ nanoparticles, J. Adv. Ceram. 6 (2017) 100.

[46] N. H. Mohammed, A. I. Abou-Aly, R. Awad, M. Rekaby, Magnetoresistance studies of Tl-1212 phase substituted by scandium, Supercond. Sci. Technol. 19 (2006) 1104.

[47] N. R. Werthamer, E. Helfand, P. C. Hohenberg, Temperature and Purity Dependence of the Superconducting Critical Field, H_{c2} III. Electron Spin and Spin-Orbit Effects, Phys. Rev. 147 (1966) 295.

[48] S. Kurnaz, B. Cakır, A. Aydiner, The effect of growth temperature on the irreversibility line of MPMG YBCO bulk with Y_2O_3 layer, Cryogenics 85 (2017) 51.

[49] W. Zhou, X. Xing, W. Wu, H. Zhao, Z. Shi, Second magnetization peak effect, vortex dynamics and flux pinning in 112-type superconductor $Ca_{0.8}La_{0.2}Fe_{1-x}Co_xAs_2$, Sci. Rep. 6 (2016) 22278.

[50] B. A. Albiss, I. M. Obaidat, M. Gharaibeh, H. Ghamlouche, S. M. Obeidat, Impact of addition of magnetic nanoparticles on vortex pinning and microstructure properties of Bi–Sr–Ca–Cu–O superconductor, Solid State Commun. 150 (2010) 1542.
[51] C. P. Bean, Magnetization of hard superconductors, Phys. Rev. Lett. 8 (1962) 250.

Table 1. Physical properties determined from magneto-resistivity measurements on all samples.

Sample	ρ_0 (mΩ.cm)	ρ_{95K} (mΩ.cm)	T_c^{onset} (K)	ΔT(K) for 0T	ΔT(K) for 6T	T_c^{offset} (K)				
						0T	1T	2T	4T	6T
0% Ag	1.85±0.09	7.61±0.38	97.6±0.5	7.3±0.7	35.9±0.7	90.3±0.5	80.5±0.5	73.1±0.5	67.0±0.5	61.6±0.5
1% Ag	1.13±0.05	3.65±0.18	97.9±0.5	6.9±0.7	34.3±0.7	91.1±0.5	82.1±0.5	74.5±0.5	68.7±0.5	63.6±0.5
3% Ag	0.25±0.02	2.54±0.13	98.7±0.5	6.7±0.7	31.3±0.7	91.9±0.5	83.8±0.5	77.6±0.5	71.0±0.5	67.4±0.5
5% Ag	1.52±0.08	4.71±0.24	98.3±0.5	6.8±0.7	32.7±0.7	91.5±0.5	82.7±0.5	76.1±0.5	69.5±0.5	65.7±0.5

Table 2. β, n, q, η, H_{irr}, and H_{c2} values for all samples

Sample	β	n	q	η	H_{irr} (0) (T)	H_{c2} (0) (T)
0% Ag	0.37±0.04	0.41±0.03	0.91±0.13	0.77∓0.05	28.9±0.8	64.6±1.4
1% Ag	0.55±0.06	0.42±0.03	1.30±0.18	0.97±0.07	30.8±0.9	74.8±2.1
3% Ag	0.45±0.01	0.44±0.03	1.03±0.07	0.89±0.03	43.1±1.3	85.9±2.5
5% Ag	0.51±0.03	0.43±0.04	1.21±0.13	0.94±0.05	39.8±1.0	80.1±2.0

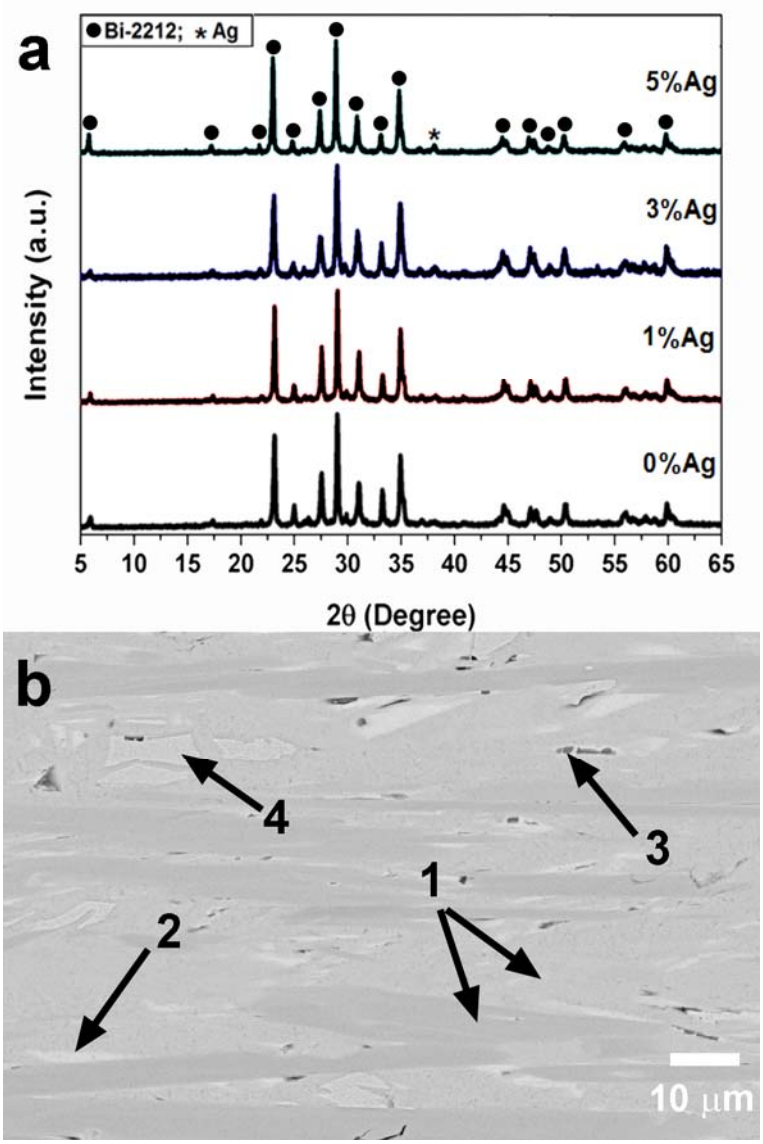

Figure 1. a) Powder XRD diffraction patterns of all samples; b) Representative SEM micrograph of 3 wt.% sample showing the different phases, #1) Bi-2212; #2) Bi-2201; #3) (Ca,Sr)CuO_2; and #4) metallic Ag.

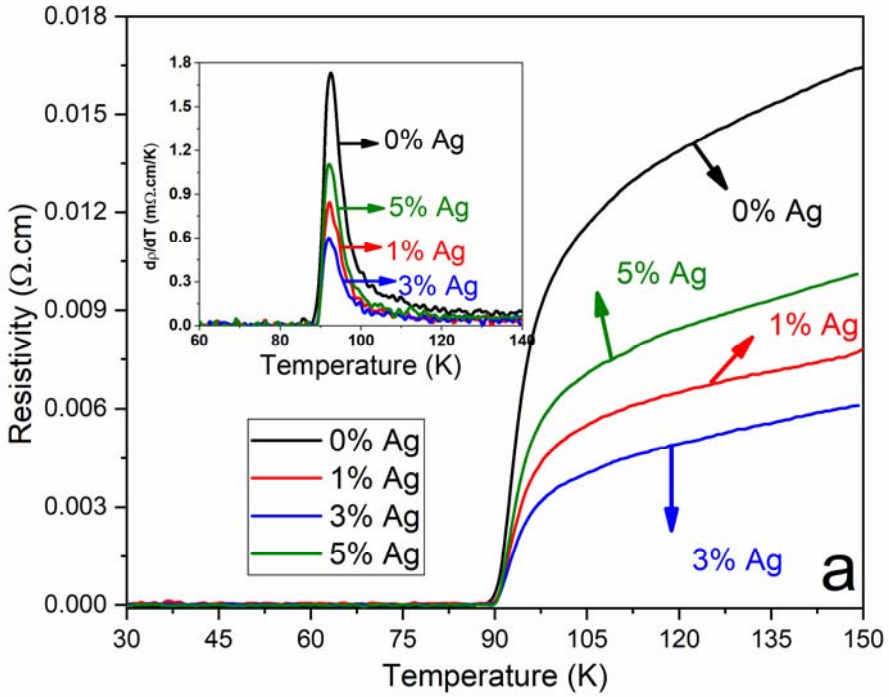

Figure 2. Variation of the dc resistivity as a function of temperature in the range 30K-150K for the $Bi_2Sr_2Ca_{0.925}Na_{0.075}Cu_2O_y$ + x wt.% Ag samples.

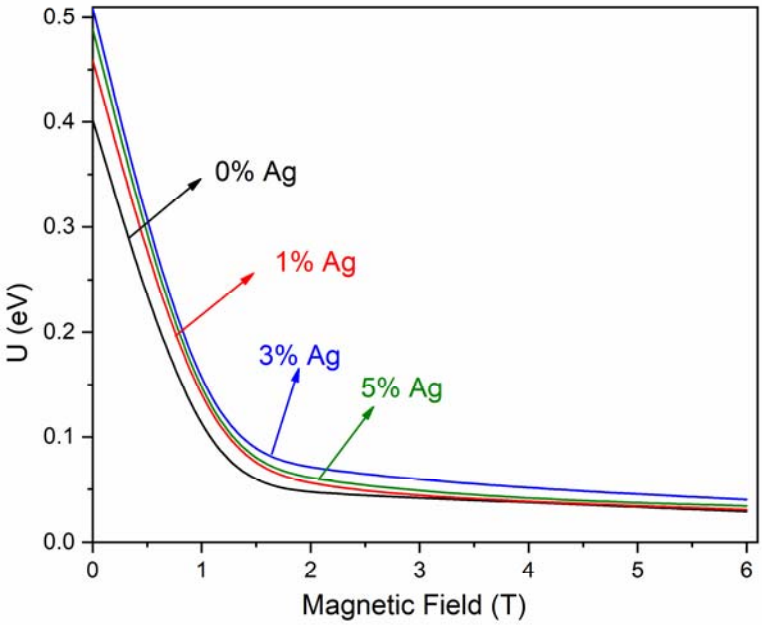

Figure 3. Variation of flux pinning energy versus applied magnetic fields up to 6 T for all samples.

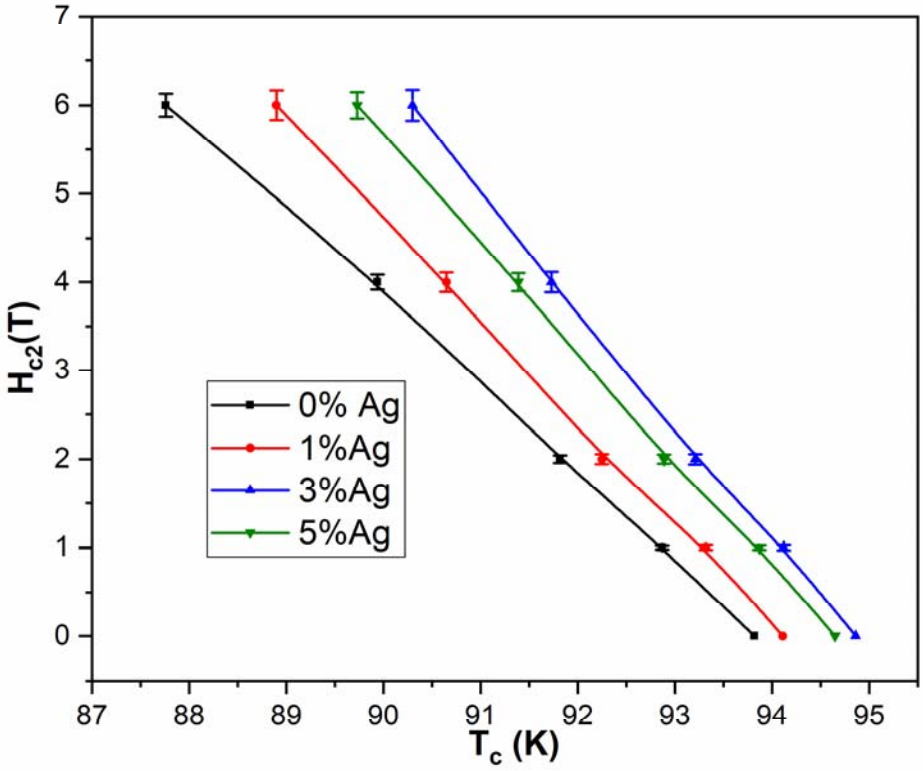

Figure 4. H_{c2} versus T_c curves, with their respective errors, for all samples.

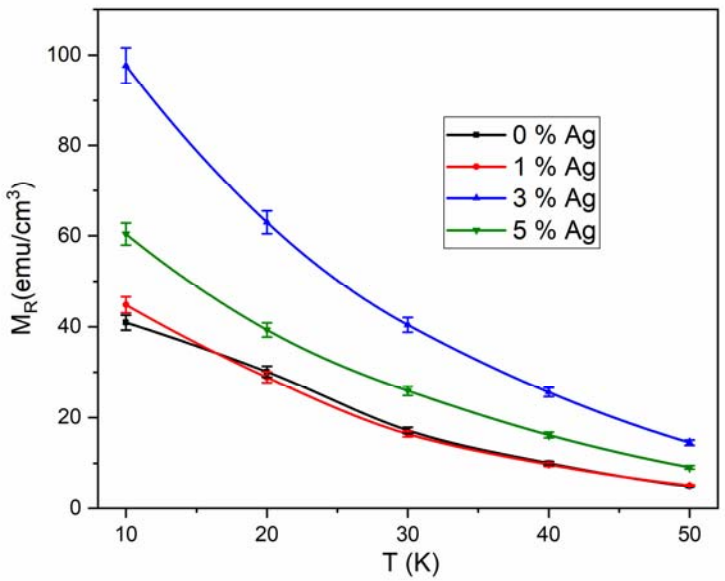

Figure 5. Variation of M_R values with temperature, with its estimated errors, for all samples.

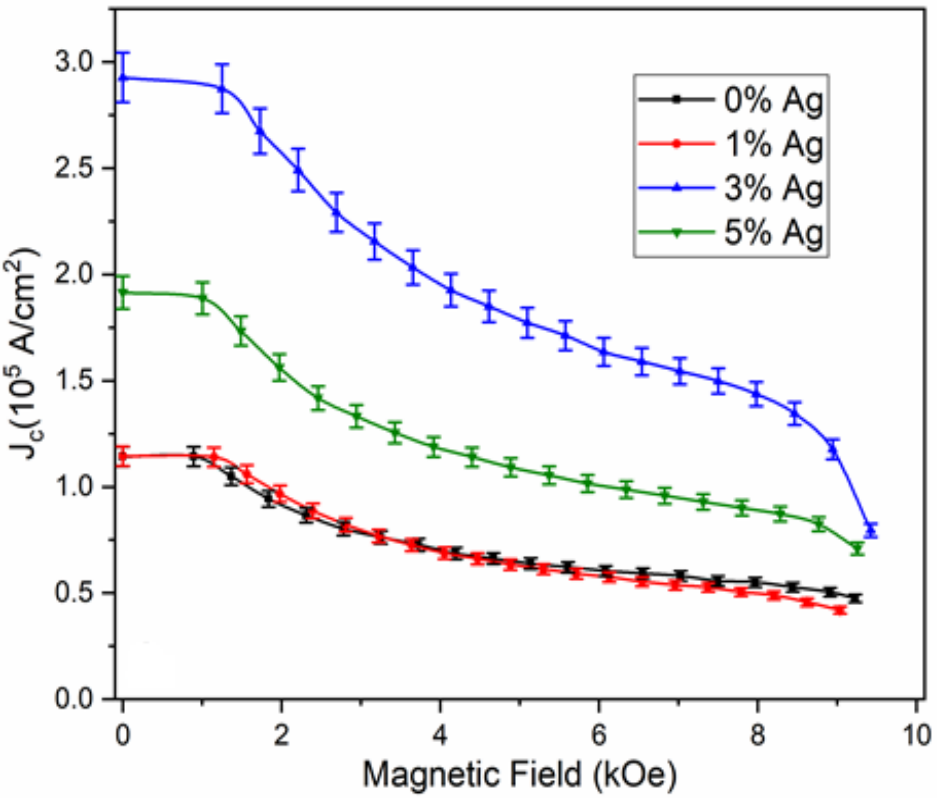

Figure 6. Calculated critical current densities (J_c) for all samples, together with their estimated errors, at 10 K.

Supporting Information

Impact of silver addition on the superconducting performances of $Bi_2Sr_2Ca_{0.925}Na_{0.075}Cu_2O_y$:Ag composite fibers

B. Atilla[1], I. Ergin[1], M. Gürsul[*1], B. Özçelik[*1], M.A. Madre[2], and A. Sotelo[2]

[1] *Department of Physics, Faculty of Sciences and Letters, Çukurova University, 01330 Adana, Turkey*

[2]*INMA (CSIC-Universidad de Zaragoza), Maria de Luna, 50018 Zaragoza, Spain*

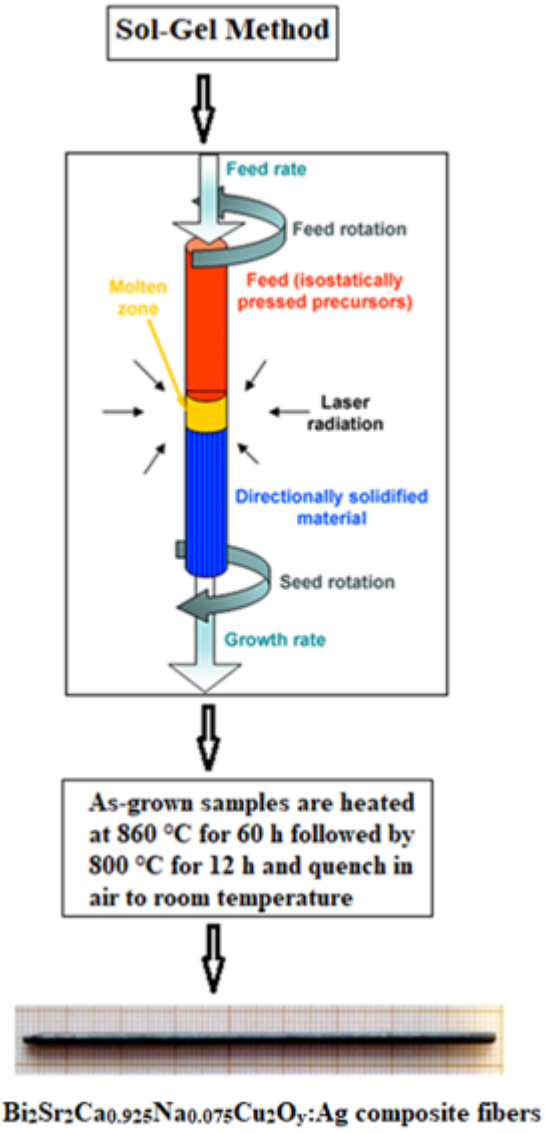

Figure S1. Schematic diagram of the experimental procedure

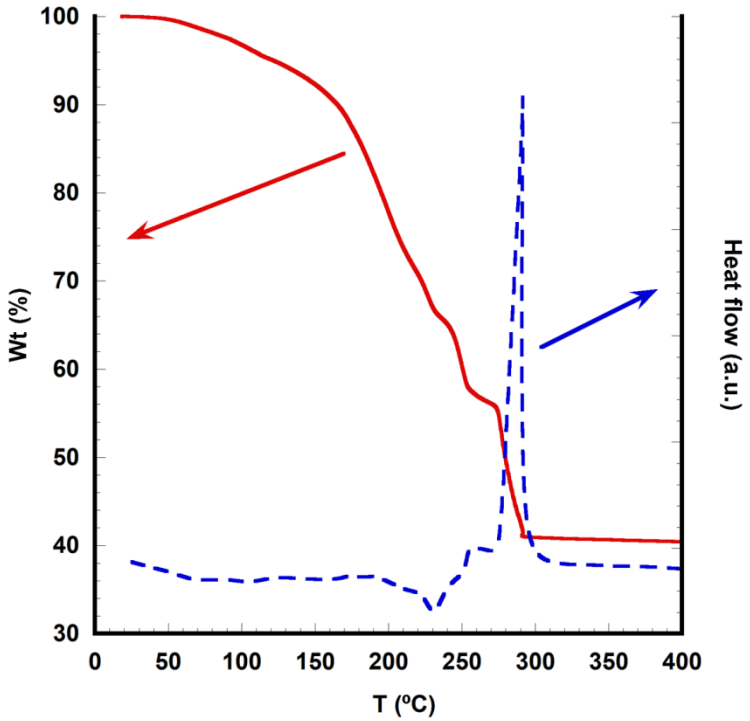

Figure S2. DTA-TGA graph of the 3 wt.% Ag dry gel.

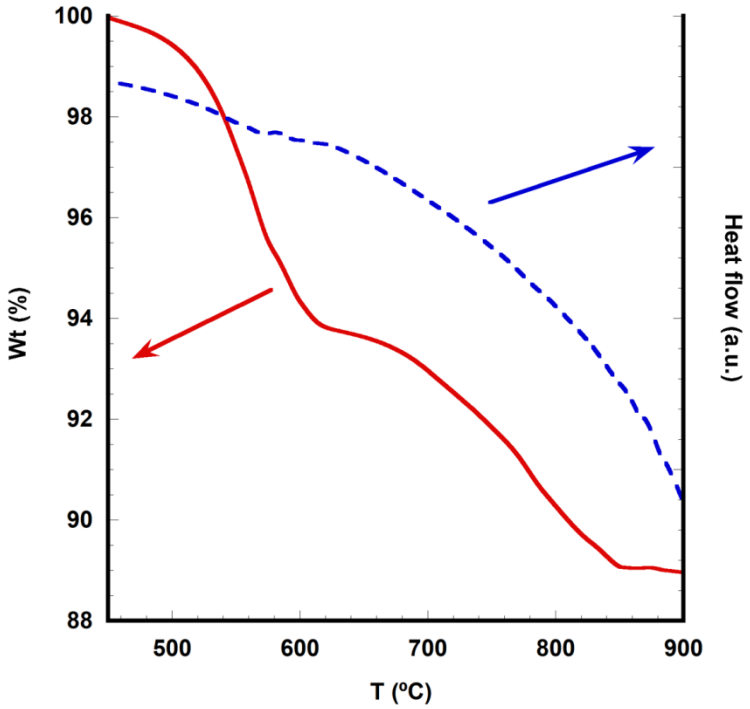

Figure S3. TGA-DTA graph performed on the 3 wt.% Ag fired powder.

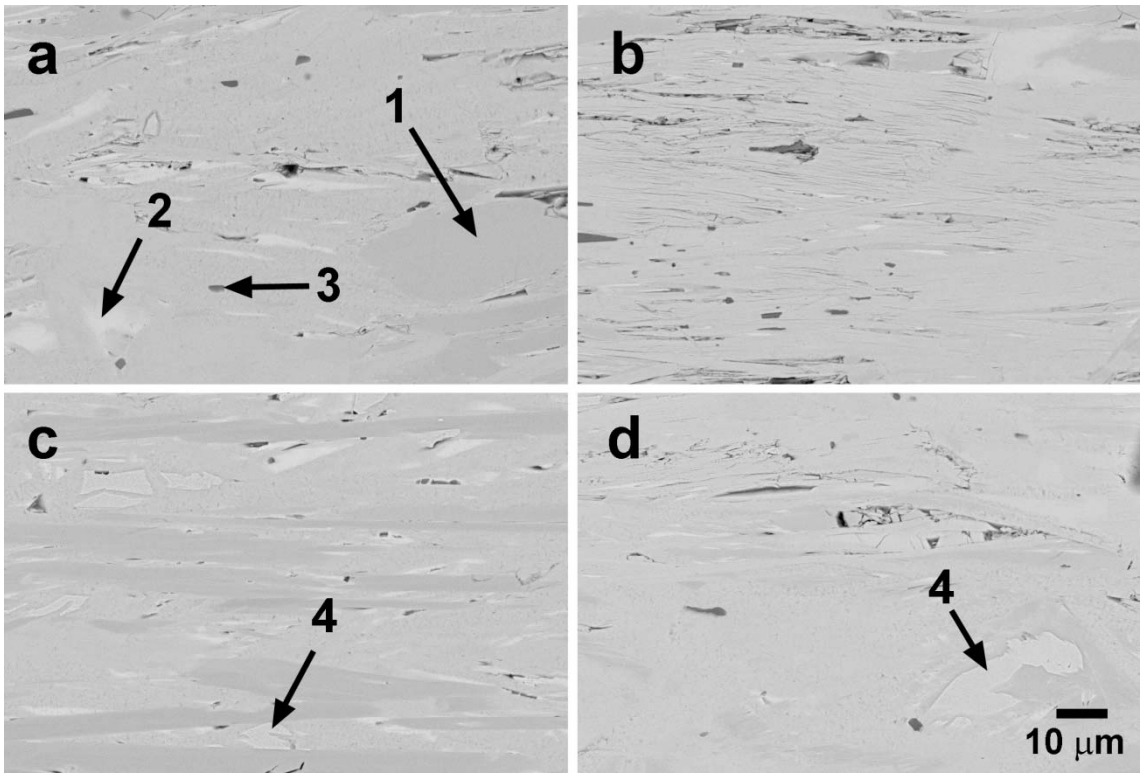

Figure S4. FESEM micrographs of polished longitudinal surfaces of $Bi_2Sr_2Ca_{0.925}Na_{0.075}Cu_2O_y$ + x wt.% Ag samples, for x **(a)** 0; **(b)** 1; **(c)** 3; and **(d)** 5. Different phases are identified with numbers #1) Bi-2212; #2) Bi-2201; #3) $(Ca,Sr)CuO_2$; and #4) metallic Ag.

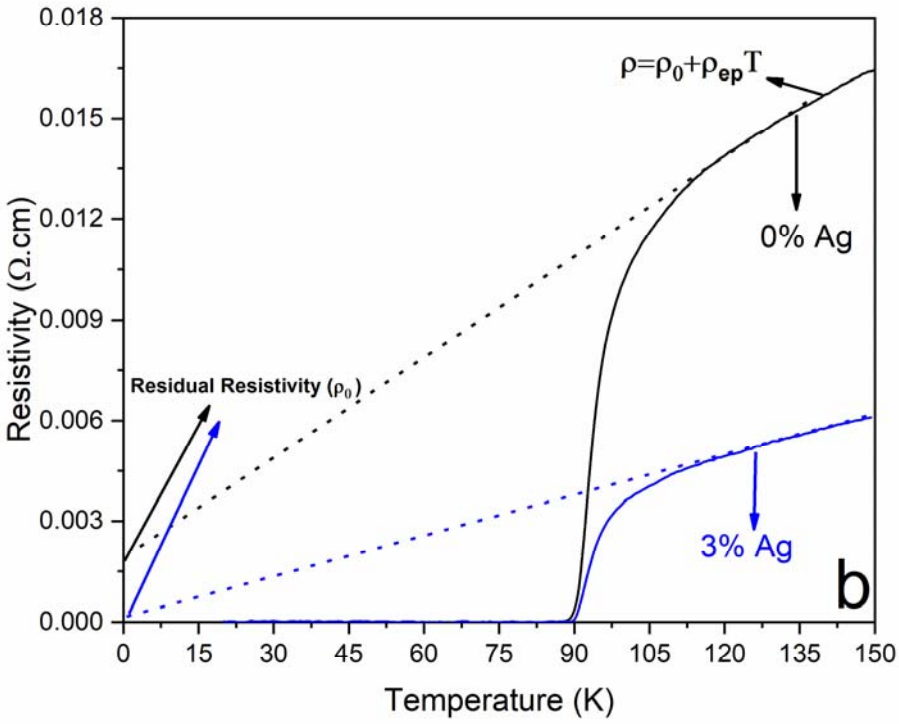

Figure S5. Values of residual resistivity for 0, and 3 wt.% Ag samples.

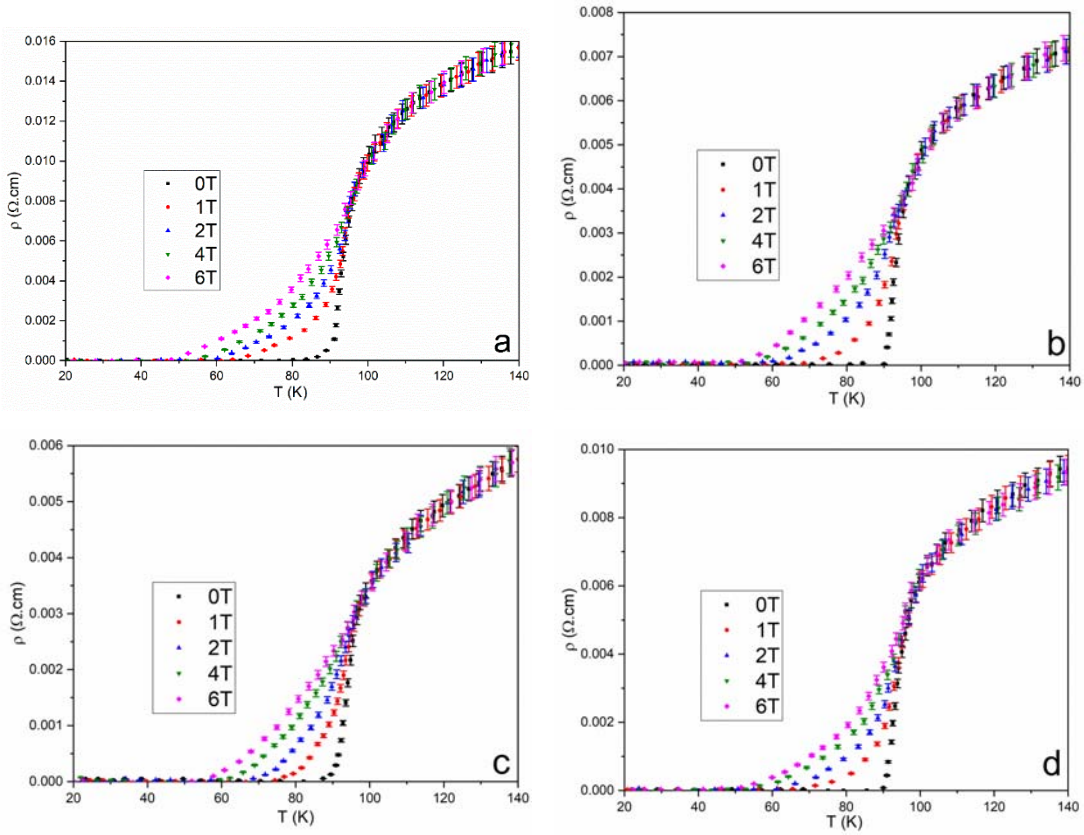

Figure S6: Variation of magneto-resistivity, together with its estimated error, with temperature under different applied magnetic fields in the range of 0-6 T for **(a)** 0, **(b)** 1, **(c)** 3 and **(d)** 5 wt.% Ag samples.

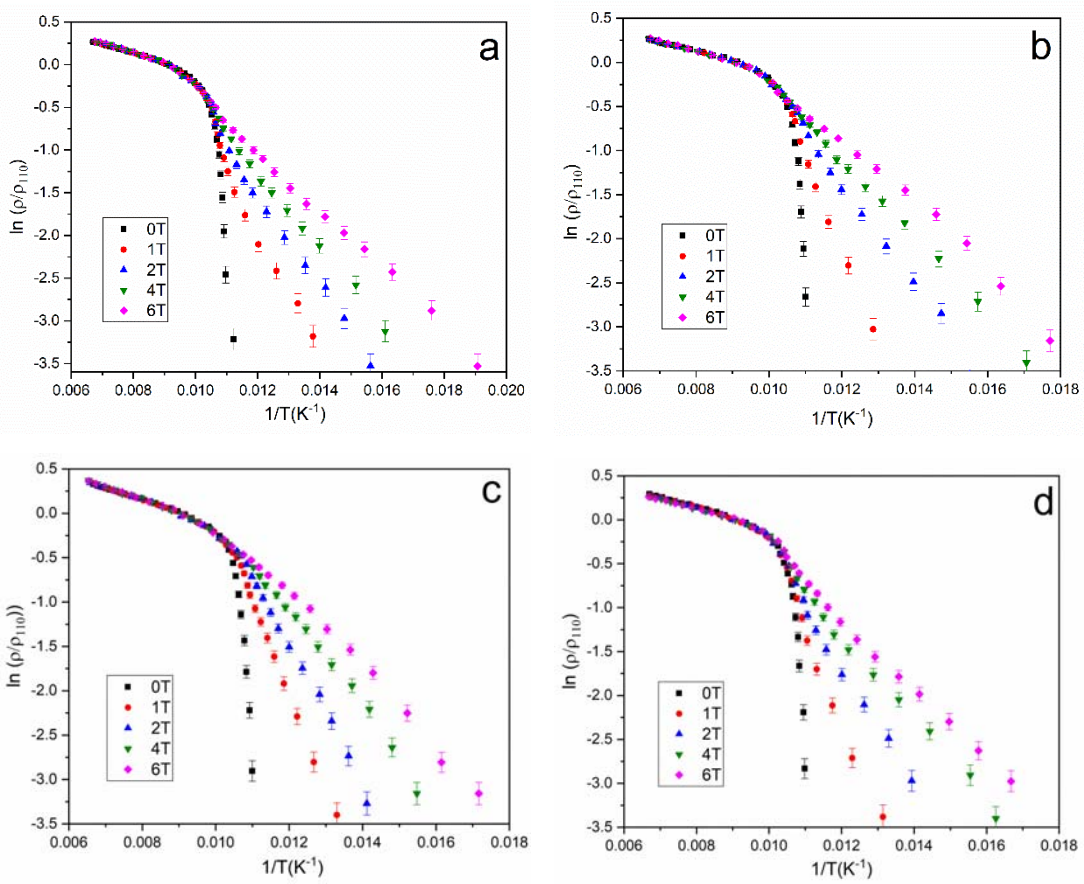

Figure S7. Arrhenius plots of the resistivity, together with their estimated error, for **(a)** 0, **(b)** 1, **(c)** 3 and **(d)** 5 wt.% Ag samples.

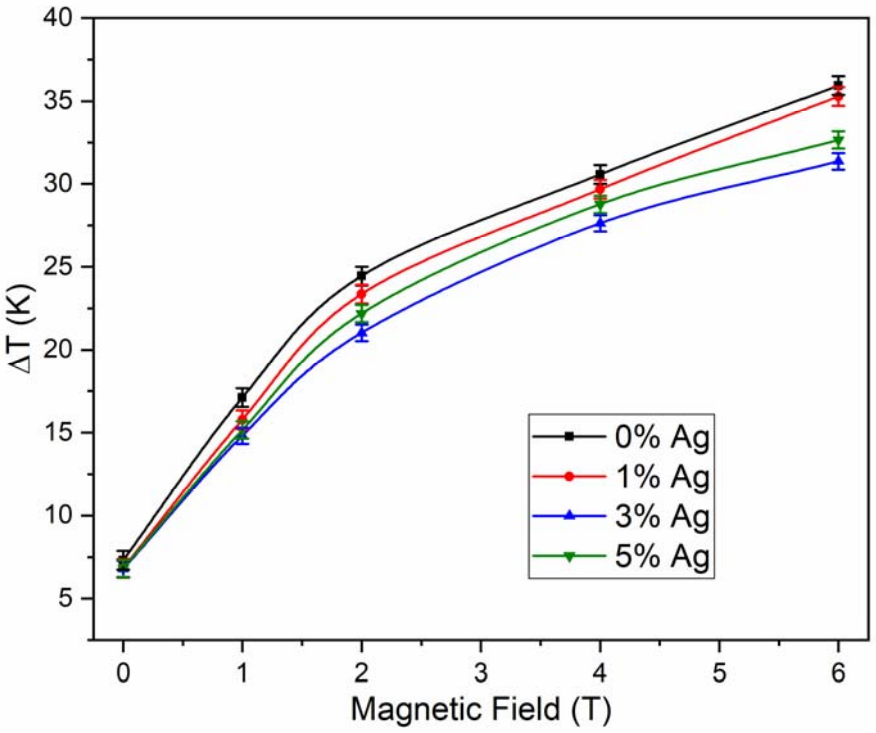

Figure S8. Variation of transition width ($\Delta T=T_c^{onset}-T_c^{offset}$) versus applied magnetic field up to 6 T, together with its estimated error, for all samples.

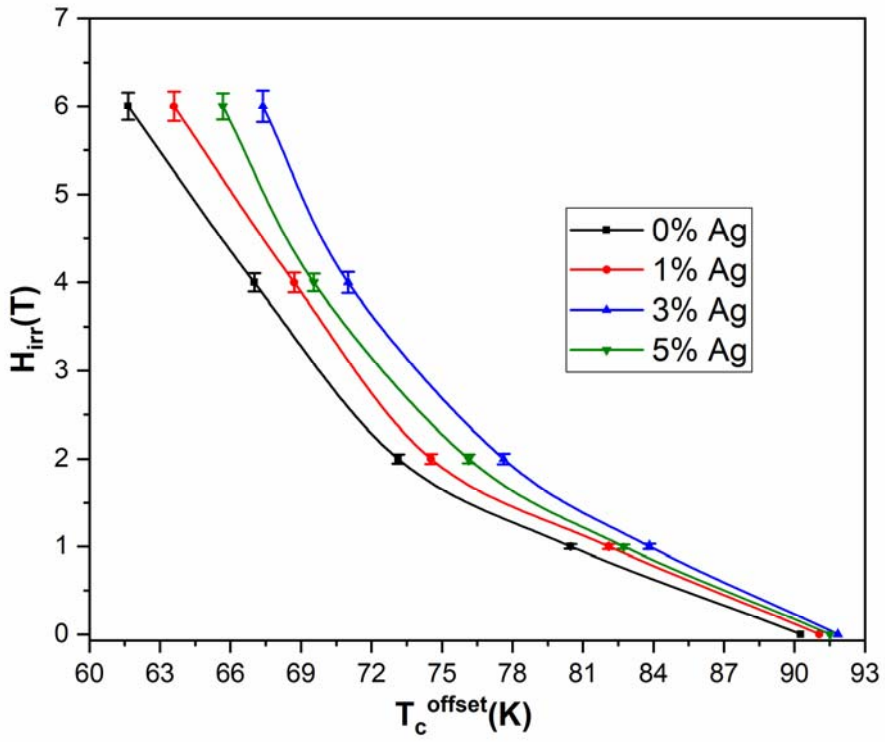

Figure S9. H_{irr} versus T_c^{offset} curves, with their estimated errors, for all samples.

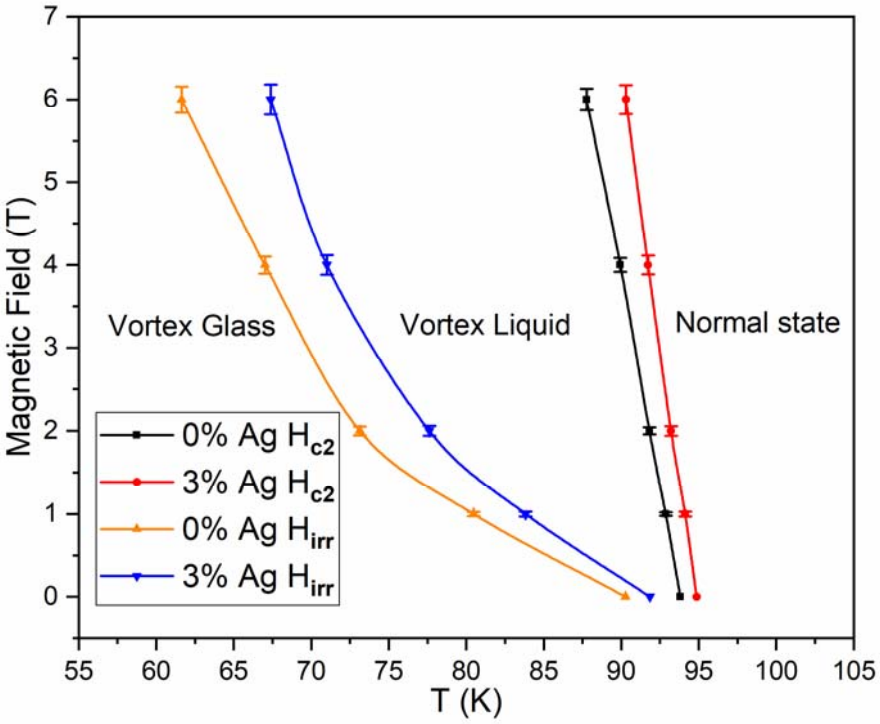

Figure S10. Vortex glass, vortex liquid and normal state determined from magneto-resistivity curves, with their estimated errors, for 0, and 3 wt.% Ag samples.

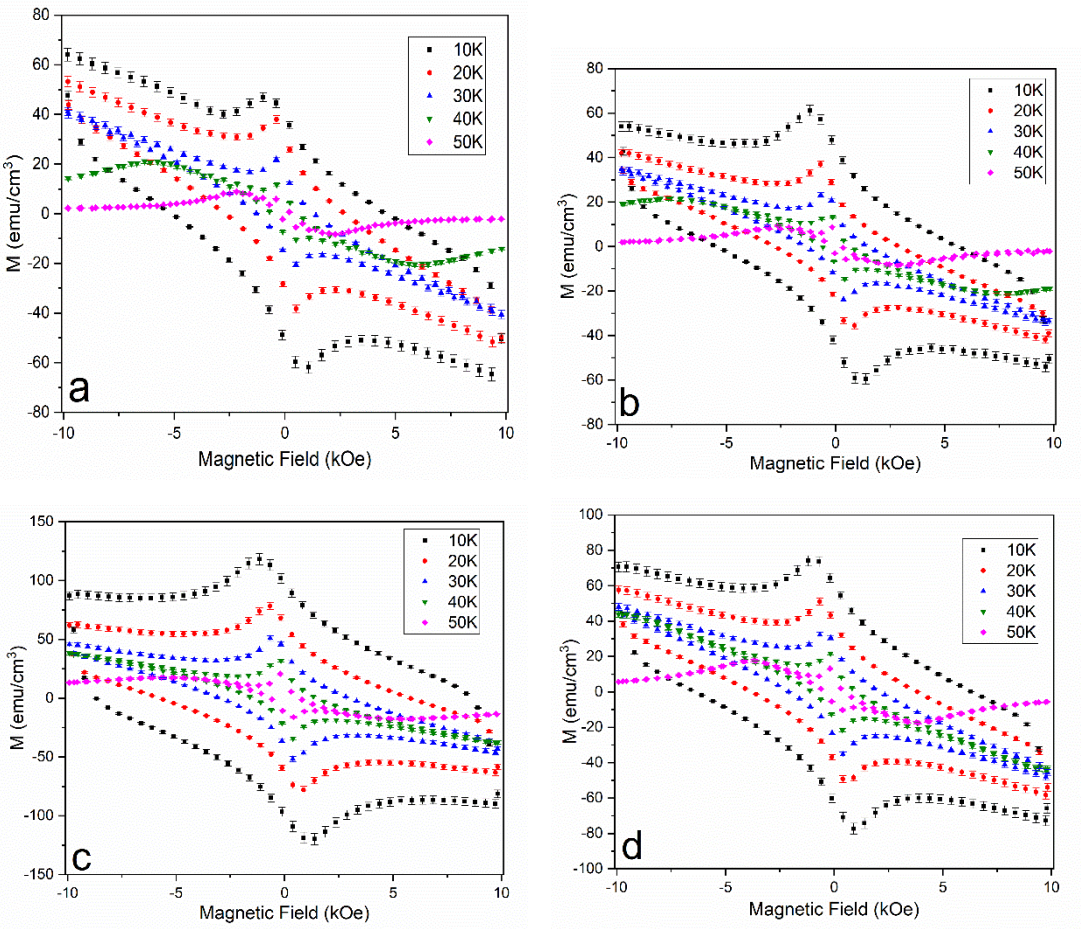

Figure S11. Magnetic hysteresis loops (M-H) of the **(a)** 0; **(b)** 1; **(c)** 3; and **(d)** 5 wt.% Ag samples under magnetic fields from -10 to +10 kOe, with their estimated errors, at different temperatures.

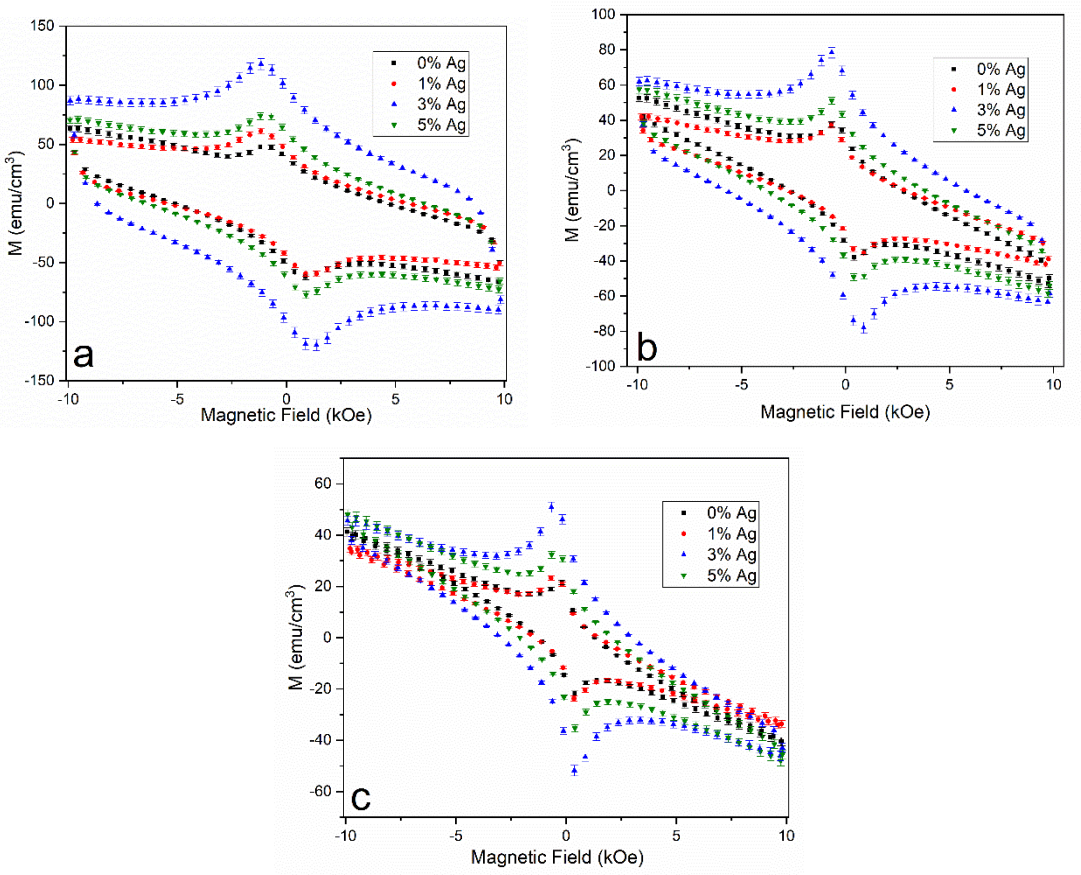

Figure S12. Magnetic hysteresis loops of all samples, with their estimated error, at **(a)** 10, **(b)** 20, and **(c)** 30 K.

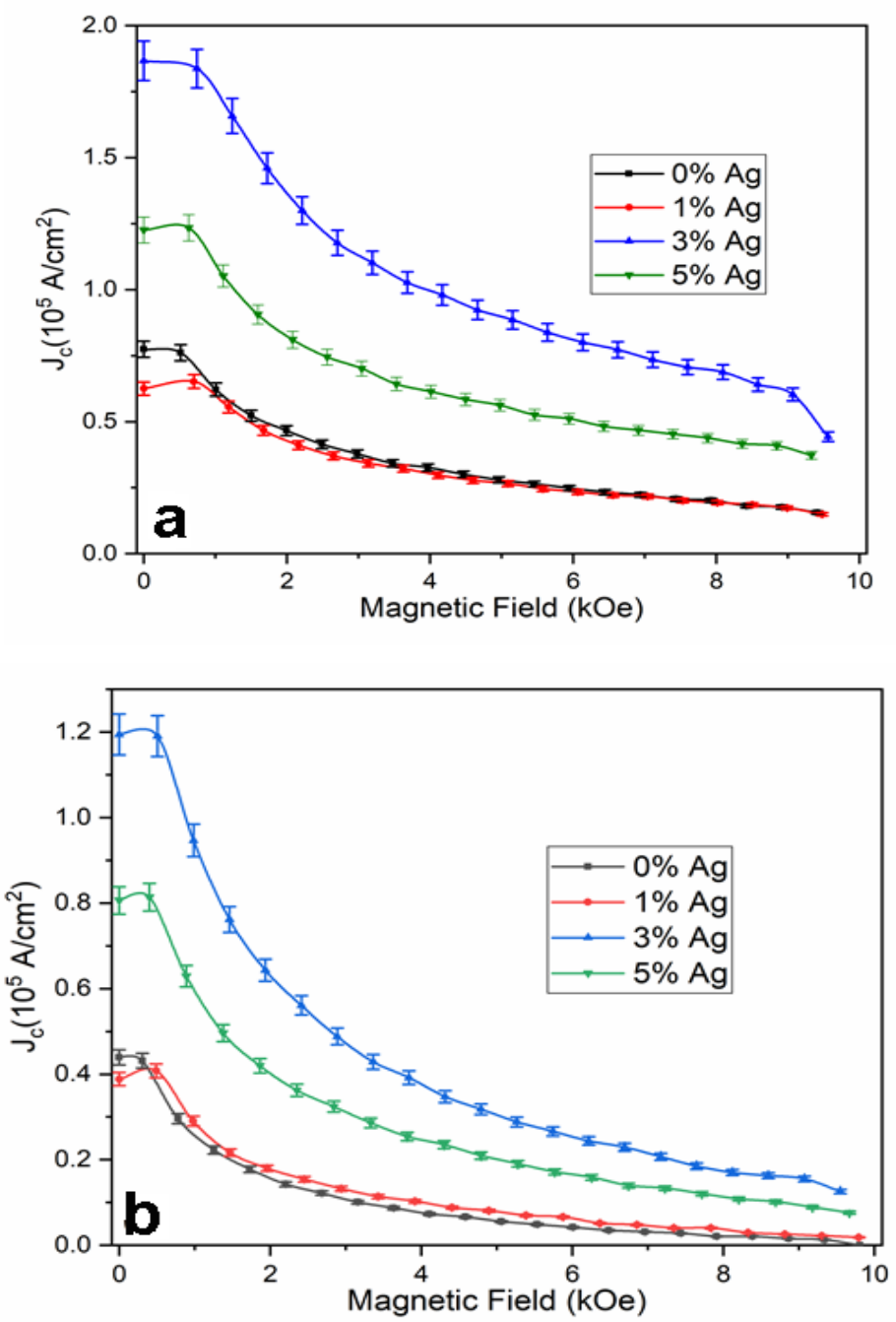

Figure S13. Calculated critical current densities (J_c) for all samples, with their estimated errors, at **(a)** 20, and **(b)** 30 K.